Reviving and Extending the Mid-Field Phase Screen Model for Distributed Aberration Correction

Rehman Ali[*], Trevor Mitcham[*], and Nebojsa Duric[*]

[*]Department of Imaging Sciences, URMC, Rochester, NY, 14620 USA

ABSTRACT

Aberration is one the key sources of image degradation in handheld B-mode ultrasound imaging. Sound speed heterogeneities in human tissue induce path-dependent delays that result in spatially varying aberrations in the image. One of the earliest models for aberration was the near-field phase screen. This was later extended to a mid-field phase screen model by introducing an offset between the aberrating screen and the transducer surface. By introducing this offset, the mid-field phase screen model could capture the parallax in the aberrations observed in the image. However, a single mid-field phase screen cannot fully capture the aberrations caused by a spatially varying sound speed. In this work, we extend the mid-field phase screen model by placing phase screens at multiple depths and demonstrate its approximate equivalence to a full sound speed profile under a straight-ray assumption. Phantom experiments show a 51-62% improvement in point target resolution because of the proposed aberration model and correction scheme.

Keywords: Sound speed estimation, differentiable beamforming, continuum mechanics, Lagrangian approach

1. INTRODUCTION

While many methods exist for phase aberration correction, they often fall short in many practical scenarios. For instance, phase screen models such as the near-field phase screen[1–3] or the midfield phase screen,[4,5] assume that all of the aberration in image can be explained by time shifts introduced at a single thin film. The near-field phase screen assumes that a single set of aberration delays acting at the transducer surface is responsible for the aberrations in the image. However, the full sound speed profile may result in aberrations delays that vary with the image point. The first model to accommodate spatial variation in the aberration delay was the mid-field phase screen, which introduced an offset between the aberrating screen and the transducer surface. Under the mid-field phase screen model, the spatial variations in the aberration delays are restricted to the parallax induced by placing the phase screen at a specific depth. However, a single screen cannot emulate the full variation in aberration delays caused by a sound speed profile that induces aberrations at multiple depths. Other approaches such as the time-reversal mirror[6] can be used to optimally focus the imaging target regardless of the sound speed distribution in tissue, but they require a physical retransmission of received ultrasound signals back into the tissue to optimally focus the imaging target. This requires real-time arbitrary waveform generation which remains infeasible for most commercial ultrasound systems to this day.

Although deviations in sound speed were always understood as the mechanism behind aberration in ultrasound imaging, the modeling and correction of aberration remained limited to the aforementioned phase screen models and time reversal approach until recent efforts to directly reconstruct the sound speed profile in tissue from phase aberrations.[7–10] These works motivated a new set of approaches to correct for aberrations in the image based on knowledge of the sound speed profile in the tissue.[10–14] However, modeling aberrations caused by the full sound speed profile has traditionally required forming a path-length matrix that computes line integrals over the entire slowness profile (i.e., reciprocal of sound speed).[8–10] Therefore, this work revisits the mid-field phase screen model with the idea of placing phase screens at multiple depths, thereby aiming to capture the full variation in aberration delay caused by a spatially varying sound speed profile. The phase screen model is revised to incorporate the impact of the incidence angle on the measured delays, and used to model aberrations induced at several depths in a differentiable beamformer.[15,16] This multi-screen approach greatly simplifies the modeling of the aberrations in the image, while offering flexibility over the number and spacing of phase screens.

Further author information: (Send correspondence to Rehman Ali)
Rehman Ali: E-mail: Rehman$_{A}li@URMC.Rochester.edu$

Medical Imaging 2026: Ultrasonic Imaging and Tomography, edited by Christian Boehm, Mohammad Mehrmohammadi, Shawn Liangzhong Xiang, Proc. of SPIE Vol. 13931, 139311N · 2026 Published by SPIE
1605-7422 · doi: 10.1117/12.3085608

2. THEORY

2.1 Revised Phase Screen Model

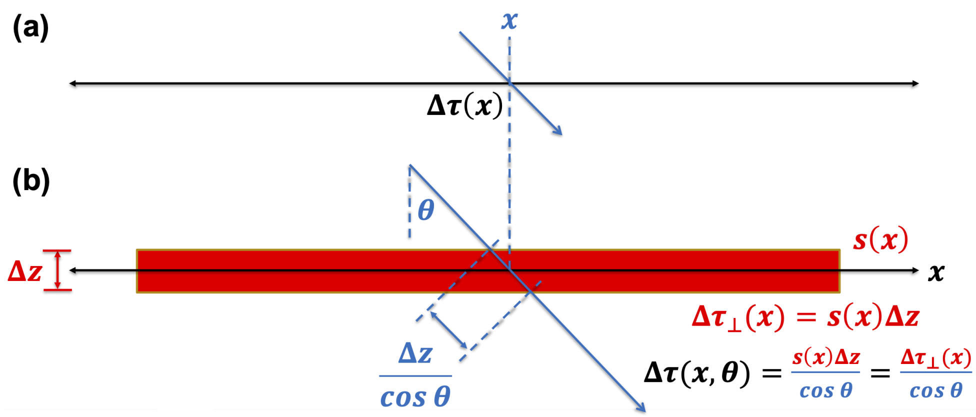

Figure 1. Phase Screen Models. (a) Original Formulation.[1–5] (b) Revised Formulation Considering the Angle of Incidence.

Under their original formulations, both the near-field[1–3] and mid-field[4,5] phase screen models were parameterized by the profile of aberration delays $\Delta\tau(x)$ over the screen (Figure 1(a)). The time-of-flight along a path that intersects the phase screen at location x accumulates an additional aberration delay $\Delta\tau(x)$ over that path, regardless of the angle of intersection. However, it can be shown that the angle of intersection will impact the aberration delay regardless of how thin the phase screen may be.

Figure 1(b) shows an infinitesimally thin slab of thickness Δz with slowness $s(x)$. If the path of sound propagation were normally incident to the phase screen, an aberration delay of $\Delta\tau_\perp(x) = s(x)\Delta z$ would be accumulated over the path. However at an angle θ (neglecting refraction), the aberration delay becomes:

$$\Delta\tau(x,\theta) = \frac{s(x)\Delta z}{\cos\theta} = \frac{\Delta\tau_\perp(x)}{\cos\theta}. \tag{1}$$

Therefore, our revised phase screen model is parameterized by the profile of aberration delays $\Delta\tau_\perp(x)$ at normal incidence, but the aberration delay accumulated along a specific path depends on θ. Both the intersection point x with the screen and the angle of incidence θ are predetermined by the start and end points of the path (e.g., the transducer element location and image point, respectively). Therefore, this simple revision adds almost no computational complexity to the phase screen model while remaining faithful to the underlying physics.

2.2 Using Multiple Mid-Field Phase Screens

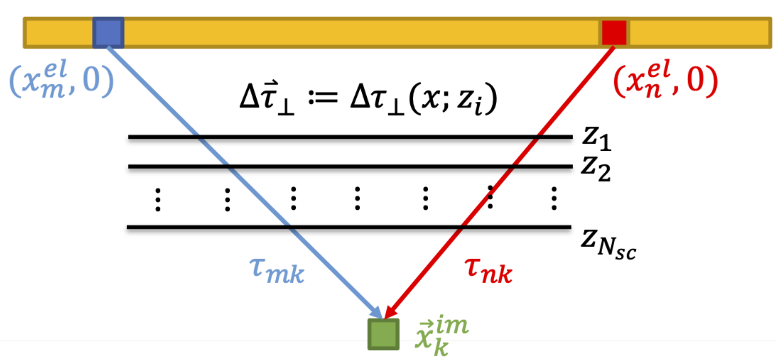

Figure 2. Delay-and-Sum Beamforming with Multiple Mid-Field Phase Screens in a Constant Sound Speed Background

Rather than use a single mid-field phase screen at a single depth, we place mid-field phase screens at multiple depths z_i ($i = 1, \ldots, N_{sc}$). This multi-screen model is parameterized by the aberration delay at normal incidence $\Delta\tau_\perp(x; z_i)$ for each phase screen. The profile of $\Delta\tau_\perp(x; z_i)$ may be converted to an equivalent slowness profile $s(x, z)$, and consequently, the sound speed profile $c(x, z)$ by considering the spacing between screens. This multi-screen approach captures the full variation in aberration delays caused by a spatially heterogeneous sound speed profile, while offering greater flexibility over the number N_{sc} and spacing $z_i - z_{i-1}$ of phase screens. In the following section, we vectorize the profile of $\Delta\tau_\perp(x; z_i)$ as $\Delta\vec{\tau}_\perp$.

2.3 Differentiable Delay-and-Sum Beamforming

The differentiable beamforming model[15,16] requires a multistatic synthetic aperture dataset $\tilde{p}_{mn}(t)$ indexed by single-element transmit m and receiver n as a function of time t. For an N-element array, let τ_{lk} refer to the time delay from element l to an image point $\vec{x}_k^{im}$. We assume a constant 1540 m/s sound speed background to calculate geometric delays. The aberration delays induced by the phase screens are added on top of the geometric delay when calculating the total delay τ_{lk}. As per Figure 2, we can focus the full matrix of transmit and receive signals at each image point $\vec{x}_k^{im}$ by applying focusing delays:

$$p_{mn}(\vec{x}_k^{im}; \Delta\vec{\tau}_\perp) = \tilde{p}_{mn}(\tau_{mk}(\Delta\vec{\tau}_\perp) + \tau_{nk}(\Delta\vec{\tau}_\perp)), \tag{2}$$

Summation over receivers yields complex-valued images for each single-element transmit:

$$I_m(\vec{x}_k^{im}; \Delta\vec{\tau}_\perp) = \sum_{n=1}^{N} p_{mn}(\vec{x}_k^{im}; \Delta\vec{\tau}_\perp). \tag{3}$$

2.4 Nonlinear Least-Squares Aberration Correction

Rather than use the common midpoint phase error approach described in,[16] we formulate aberration correction as a nonlinear least-squares problem[15] with the following objective function:

$$E(\Delta\vec{\tau}_\perp) = \frac{1}{2} \sum_k \sum_{m=1}^{N-1} \left| I_{m+1}(\vec{x}_k^{im}; \Delta\vec{\tau}_\perp) - I_m(\vec{x}_k^{im}; \Delta\vec{\tau}_\perp) \right|^2. \tag{4}$$

This direct error avoids the pitfalls phase error minimization in the anechoic regions of the image. The multiple mid-field phase screen model, differentiable beamformer, and objective function above were implemented using the automatic differentiation software known as JAX.[17] The conjugate gradient algorithm (50 iterations total) was used to minimize $E(\Delta\vec{\tau}_\perp)$ based on gradients calculated by JAX.

3. METHODS

3.1 Imaging Studies: Experimental and Simulation

All imaging in this study was performed using a Verasonics Vantage 256 ultrasound system (Verasonics Inc., Kirkland, WA, USA) with an 8 MHz center-frequency L12-5 50mm transducer (Advanced Technology Laboratories, Inc., Bothell, WA, USA). Hadamard pulse sequences were used to maximize signal-to-noise ratio. The multi-screen model applied to this data consist of 10 equally spaced mid-field phase screens from 1 to 19 mm in depth. Additional imaging studies based on simulation work in k-Wave[18] involves placing 25 mid-field phase screens placed from 1 to 25 mm equally spaced in depth.

3.2 Phantom Fabrication

All tissue-mimicking phantoms in this work were fabricated with 8% gelatin (SigmaAldrich, St. Louis, MO, USA), 2.5% silica (US Silica, Katy, TX, USA), 89.4% deionized water, and 0.1% glutaraldehyde (SigmaAldrich). Point targets which consisted of 36-GA (250-µm diameter) wire (McMaster-Carr) were included as imaging targets within all phantoms. To this end, 6/16-inch diameter holes were drilled on opposite sides of a 4-inch acrylic 5-sided cube so that the wires could be inserted in a repeatable manner. Additionally, hypo-echoic lesions consisting of 8% gelatin, 0.5% silica, 91.4% deionized water, and 0.1% glutaraldehyde were included in several phantoms. These inclusions were cast by drilling 6/16-inch diameter holes below the wire inclusions on one side, inserting a closed tube while pouring the gelatin background, and then back-filling the negative space after the tube's removal. Gelatin inclusions with an increased sound speed were also cast above the wire targets in several phantoms using a similar technique, but using 8% gelatin, 2.5% silica, 69.4% deionized water, 20% isopropanol, and 0.1% glutaraldehyde to fill the negative space. Figure 3 visually shows the two phantoms constructed using this process to test the aberration correction technique.

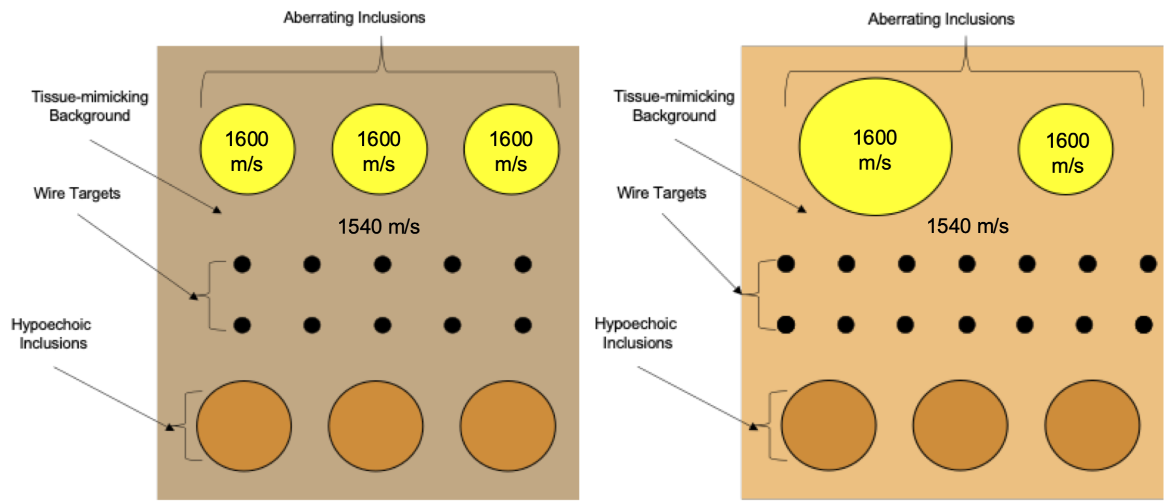

Figure 3. Visual Schematic of Aberration Phantom Constructions. (Left) Three evenly spaced high-sound-speed inclusions with equal radius. (Right) Two asymmetric high-sound speed inclusions with one inclusion larger than the other.

4. RESULTS AND DISCUSSION

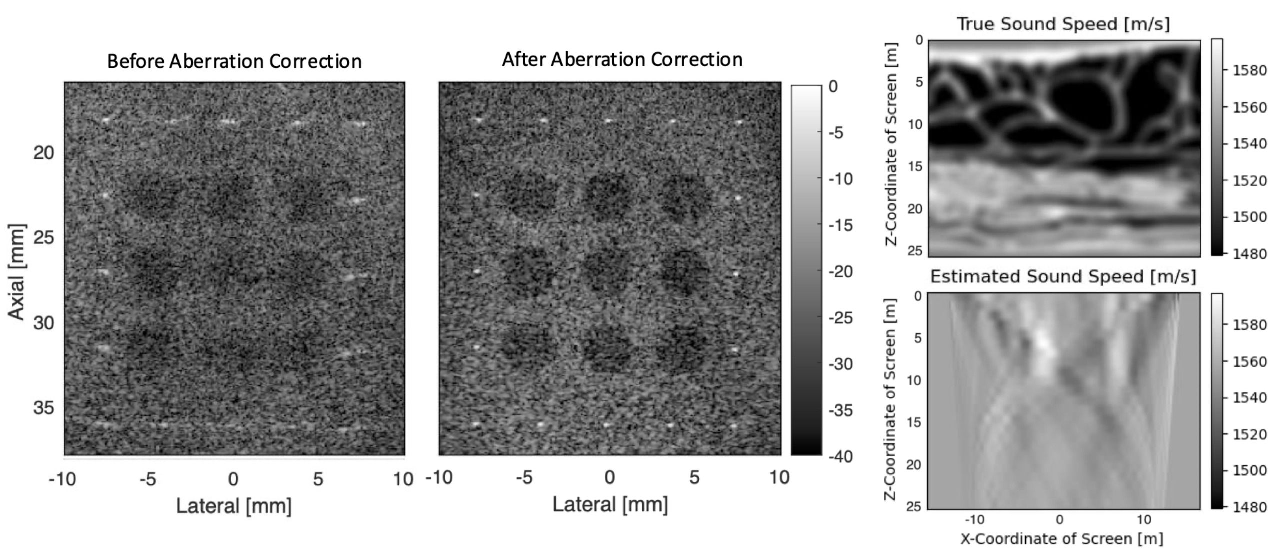

Figure 4. Sound Speed Estimation and Phase Aberration Correction Based on a Multiple Mid-Field Phase Screen Model in k-Wave Simulation.[18] When using a homogenous 1540 m/s sound speed to reconstruct the B-mode image, the full width at half maximum (FWHM) resolution of the image targets at 36 mm depth are 2.19 ± 0.92 mm. Using the multi-screen correction improves the FWHM resolution to 0.31 ± 0.03 mm.

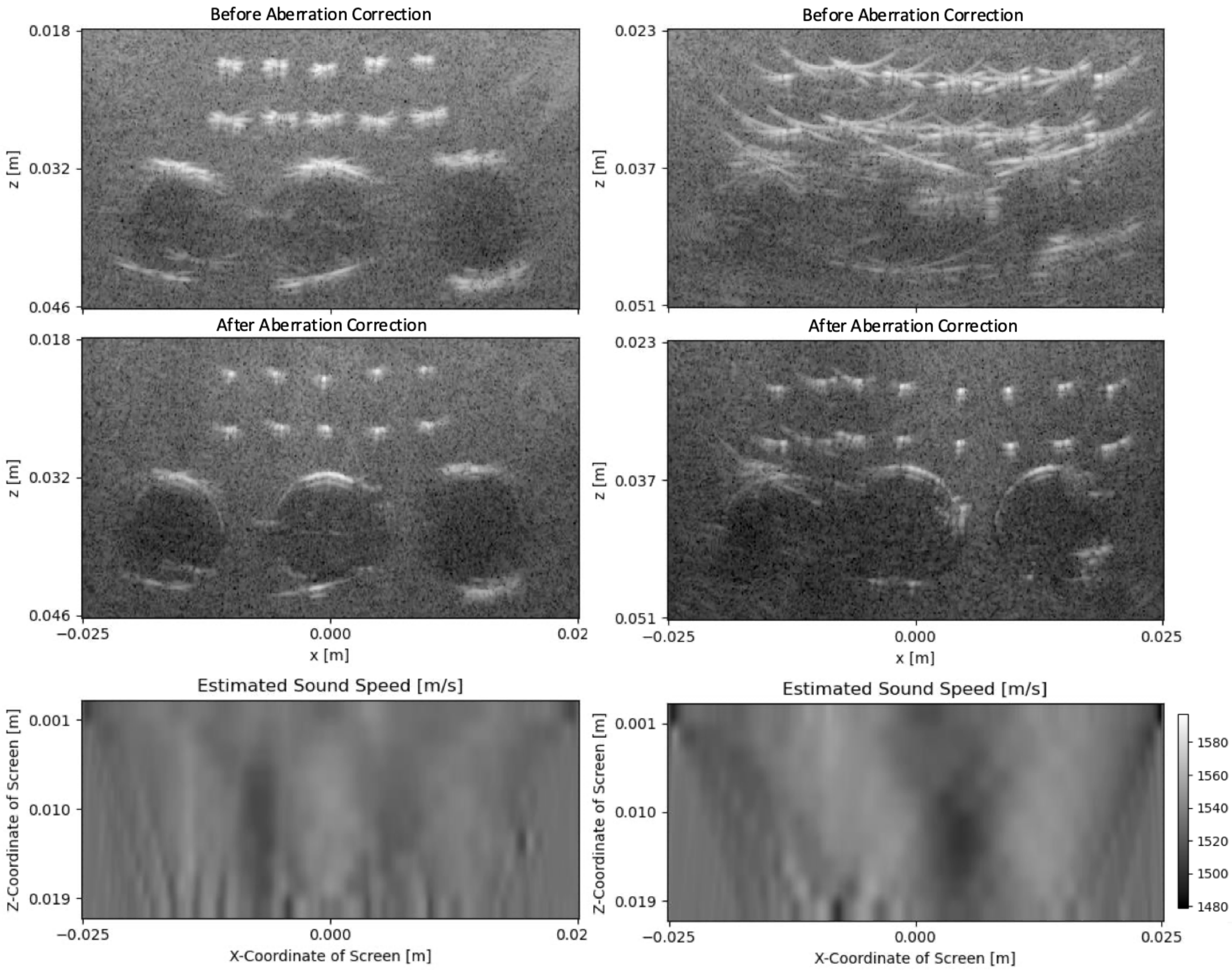

Figure 5. Sound Speed Estimation and Phase Aberration Correction Based on a Multiple Mid-Field Phase Screen Model in Phantom Experiments. In the phantom on the left, the full width at half maximum (FWHM) resolution decreases from 1.25 ± 0.56 mm to 0.45 ± 0.21 mm, which is a $61.79 \pm 18.97\%$ improvement in point target resolution. In the phantom on the right, the FWHM decreases from 2.81 ± 1.88 mm to 0.8103 ± 0.7545 mm, which is a $51.71 \pm 17.91\%$ improvement in point target resolution.

The k-Wave[18] simulations used in prior work[10] were reused here to provide an initial demonstration of sound speed estimation and aberration correction using the multiple mid-field phase screen model. The simulations in Figure 4 show that the full width at half-maximum (FWHM) resolution improves from 2.19 $\pm$ 0.92 mm to 0.31 $\pm$ 0.01 mm. The mid-field phase screens at each depth capture the laterally varying component of the sound speed distribution responsible for the aberrations observed in the image at an initial beamforming sound speed of 1540 m/s.

Accurate tissue-mimicking phantoms can be fabricated using the methods described herein, both regarding sound speed and echogenicity. The 20% isopropyl alcohol inclusions provide a significant increase in sound speed (i.e., greater than 1600 m/s) relative to the background gelatin material (approximately 1540 m/s) which causes high levels of aberration in both point targets and hypoechoic targets. Figure 5 shows aberration correction in phantoms based on the estimated $\Delta\tau_{\perp}(x; z_i)$ converted to sound speed for visualization purposes. These sound speed profiles, for the phantoms on the left and right, show three and two inclusions, respectively. For the phantom on the left and right, the improvement in point target resolution is 61.79 $\pm$ 18.97% and 51.71 $\pm$ 17.91%, respectively.

These results show that a moderate number of mid-field screens (25 shown in the k-Wave simulation and 10 in phantom experiments) can effectively model the full set of aberrations caused by a spatially-varying sound speed map. Although this work uses the mid-field phase screen model in a differentiable beamformer, the same set of multiple mid-field phase screens could be used to simplify the modeling of aberrations delays measured using cross-correlation[10] or phase-shift[9] techniques outside of differentiable beamforming. Although not exploited here, non-uniform depth placements can be used strategically to reduce model size while capturing all the relevant aberrations. This flexible and versatile modeling of aberration delay can be used in point-of-care ultrasound (POCUS) systems to simplify aberration correction, especially with limited computational resources.

Alternatively, the idea of differentiable beamforming[15,16] may be adopted within POCUS. As investigated so far, differentiable beamforming has been used to converge to the ideal sound speed estimates and aberration corrections over many iterations (e.g., 100[15]-200[16]) for individual image frames. Although this work greatly simplifies the inverse problem, a significant number of iterations (50) is still required for convergence, remaining a challenge for real-time imaging. Explicit linearized inversion at each iteration may reduce the number of iterations and reduce computational cost if the number of model parameters is kept small enough.

However, such improvements may not be sufficient if the number of iterations required for convergence at each imaging frame cannot be reduced far enough. Therefore, rather than converge to the optimal aberration correction for each image frame separately, adaptive filtering techniques such as the least-mean-squares (LMS) algorithm or the Kalman filter may be used to estimate the parameters of the multi-screen model over multiple frames. In essence, this would significantly reduce the computational burden on a single image frame and distribute it over multiple frames. The goal would be to keep the number of image frames needed for convergence (i.e., the settling time, lag, or time constant) within a tolerable range that accommodates tissue or probe motion without sacrificing the frame-rate needed for real-time POCUS imaging.

5. CONCLUSIONS

We present an iterative aberration correction scheme for handheld pulse-echo ultrasound based on modeling mid-field phase screens at multiple depths in the medium. This simplified model can be used in lieu of a complete sound speed map and can accurately capture aberrations caused by large lateral variations in the speed of sound. This work demonstrates that a multiple mid-field phase screen model can iteratively estimate and correct for aberrations in the ultrasound image. Aberration correction in phantoms shows a 51-62% improvement in point target resolution. The main advantage of this new correction scheme relative our prior work[15] is its simplified modeling of aberration delays in a laterally varying sound speed medium.

ACKNOWLEDGMENTS

This work was supported by the National Institute of Biomedical Imaging and Bioengineering (NIBIB) from the National Institute of Health (NIH) under grants F32-EB034589 and K99-EB037080.

REFERENCES

[1] Li, Y., "Phase aberration correction using near-field signal redundancy. i. principles [ultrasound medical imaging]," *IEEE transactions on ultrasonics, ferroelectrics, and frequency control* **44**(2), 355–371 (1997).

[2] Dahl, J. J., McAleavey, S. A., Pinton, G. F., Soo, M. S., and Trahey, G. E., "Adaptive imaging on a diagnostic ultrasound scanner at quasi real-time rates," *IEEE transactions on ultrasonics, ferroelectrics, and frequency control* **53**(10), 1832–1843 (2006).

[3] Mozaffarzadeh, M., Verweij, M. D., de Jong, N., and Renaud, G., "Comparison of phase-screen and geometry-based phase aberration correction techniques for real-time transcranial ultrasound imaging," *Applied Sciences* **12**(19), 10183 (2022).

[4] Tillett, J. C., Astheimer, J. P., and Waag, R. C., "A model of distributed phase aberration for deblurring phase estimated from scattering," *IEEE transactions on ultrasonics, ferroelectrics, and frequency control* **57**(1), 214–228 (2009).

[5] Liu, D.-L. and Waag, R. C., "Correction of ultrasonic wavefront distortion using backpropagation and a reference waveform method for time-shift compensation," *The Journal of the Acoustical Society of America* **96**(2), 649–660 (1994).

[6] Fink, M., "Time reversal of ultrasonic fields. i. basic principles," *IEEE transactions on ultrasonics, ferroelectrics, and frequency control* **39**(5), 555–566 (1992).

[7] Jaeger, M., Held, G., Peeters, S., Preisser, S., Grünig, M., and Frenz, M., "Computed ultrasound tomography in echo mode for imaging speed of sound using pulse-echo sonography: proof of principle," *Ultrasound in medicine & biology* **41**(1), 235–250 (2015).

[8] Rau, R., Schweizer, D., Vishnevskiy, V., and Goksel, O., "Speed-of-sound imaging using diverging waves," *International Journal of Computer Assisted Radiology and Surgery* **16**(7), 1201–1211 (2021).

[9] Stähli, P., Kuriakose, M., Frenz, M., and Jaeger, M., "Improved forward model for quantitative pulse-echo speed-of-sound imaging," *Ultrasonics* **108**, 106168 (2020).

[10] Ali, R., Mitcham, T. M., Singh, M., Doyley, M. M., Bouchard, R. R., Dahl, J. J., and Duric, N., "Sound speed estimation for distributed aberration correction in laterally varying media," *IEEE transactions on computational imaging* **9**, 367–382 (2023).

[11] Rau, R., Schweizer, D., Vishnevskiy, V., and Goksel, O., "Ultrasound aberration correction based on local speed-of-sound map estimation," in [*2019 IEEE International Ultrasonics Symposium (IUS)*], 2003–2006, IEEE (2019).

[12] Jiang, C., Li, Y., Li, B., Liu, C., Xu, F., Xu, K., and Ta, D., "Ray theory-based transcranial phase correction for intracranial imaging: A phantom study," *IEEE Access* **7**, 163013–163021 (2019).

[13] Jiang, C., Li, Y., Xu, K., and Ta, D., "Full-matrix phase shift migration method for transcranial ultrasonic imaging," *IEEE Transactions on Ultrasonics, Ferroelectrics, and Frequency Control* **68**(1), 72–83 (2020).

[14] Schwab, H.-M., Ihrig, A., Depke, D., Hermann, S., Schäfers, M., and Schmitz, G., "Aberration correction in photoacoustic imaging using paraxial backpropagation," in [*2017 IEEE International Ultrasonics Symposium (IUS)*], 1–4, IEEE (2017).

[15] Ali, R., Mitcham, T., Singh, M., Bouchard, R., Doyley, M., Dahl, J., and Duric, N., "Iterative sound speed tomography for distributed aberration correction," in [*2023 IEEE International Ultrasonics Symposium (IUS)*], 1–4, IEEE (2023).

[16] Simson, W., Zhuang, L., Frey, B. N., Sanabria, S. J., Dahl, J. J., and Hyun, D., "Ultrasound autofocusing: Common midpoint phase error optimization via differentiable beamforming," *IEEE Transactions on Medical Imaging* (2025).

[17] Bradbury, J., Frostig, R., Hawkins, P., Johnson, M. J., Leary, C., Maclaurin, D., Necula, G., Paszke, A., VanderPlas, J., Wanderman-Milne, S., et al., "Jax: Autograd and xla," *Astrophysics Source Code Library* , ascl–2111 (2021).

[18] Treeby, B. E. and Cox, B. T., "k-wave: Matlab toolbox for the simulation and reconstruction of photoacoustic wave fields," *Journal of biomedical optics* **15**(2), 021314–021314 (2010).